Volume 1 | Number 1 | Jan 2013 | Pages 1–100

Journal of
Materials Chemistry B

Materials for biology and medicine
www.rsc.org/materialsB

ROYAL SOCIETY OF CHEMISTRY

ROYAL SOCIETY OF CHEMISTRY

www.rsc.org/materialsB

Journal Name

ARTICLE

Tailoring the Biological Response of Mesoporous Bioactive Materials

N. Gómez-Cerezo[a,b], I. Izquierdo-Barba[a,b], D. Arcos[a,b]*and M. Vallet-Regí[a,b]*

Mesoporous bioactive glasses (MBGs) in the system SiO_2-CaO-P_2O_5 have been prepared using different non-ionic structure directing agents (SDA): Brij58, F68, P123 and F127. For the first time, the bioactive response of MBGs can be tailored with the kind of SDA incorporated. This is because, in addition to the textural properties, we can use the SDA to tailor the local atomic environment within the MBGs struts. These features lead to differences in the in vitro bioactive behaviour of MBGs. Among the different SDAs used in this work, the triblock copolymer F68 leads to MBGs that exhibit the fastest bioactivity and the fastest differentiation induction from pre-osteoblast towards osteoblast phenotype. These results are explained in terms of a highly ordered mesoporous structure, more free calcium cations acting as silica network modifiers and small mesopores that avoid the formation of CaP nuclei within pores, which could obstruct the ionic exchange with the surrounding fluids.

Introduction

Mesoporous bioactive glasses (MBGs) are a new generation of bioceramics intended for regenerative therapies of bone [1,2]. They comprise the bone bonding capabilities of both, melt-derived and sol-gel bioactive glasses [3,4], and the porous structure of SiO_2 based mesoporous materials [5,6]. The addition of both characteristics results in a synergy from the point of view of their biomedical applications. First, the high surface areas and porosities enhance the bioactive behavior, as the reactivity with the physiological fluids is greater and faster [7,8]. Secondly, the mesoporous ordering makes these materials excellent matrixes as drug delivery systems [9-12].

MBGs were firstly proposed by Yan et al in the SiO_2-P_2O_5-CaO system [13]. These ternary compositions have been the most widely studied for MBGs and conventional sol-gel bioactive glasses [14-17]. In this system, SiO_2 and P_2O_5 are added as network formers and CaO is incorporated to the system as network modifiers [18,19]. When bioglasses are soaked in simulated body fluid (SBF) [20], the Ca^{2+} cations are leached and initiate the sequence of reactions described by Hench [21]. These events begin with the Ca^{2+}- H^+ exchange with the surrounding fluid and result in the nucleation and growth of an apatite-like layer onto the materials surface. Kokubo et al [22] stated that those materials that develop an apatite phase when soaked in SBF under in vitro conditions, will exhibit bone bonding and/or regeneration capabilities in vivo. This statement is widely accepted by a large part of scientific community,

although some criticism about the scientific evidence for this assumption has been reported [23]. Anyway, since bioactivity is as surface process, the higher surface area and porosity is considered the main factors for the enhanced bioactivity of MBGs respect to conventional bioglasses [24-26].

The interest for MBGs has impelled to different research teams to explore alternatives for upgrading their characteristics. For instance, Li et al have studied the incorporation of dopants into MBGs such as Mg, Zn or Cu [27]. Wu et al have evaluated the biological meaning of Sr [28,29], B [30] as well as Co [31] and Cu [32] to mimic hypoxia conditions and Salinas et al have also studied the incorporation of cerium, gallium and zinc [33,34]. In addition to the incorporation of new elements into the glassy network, other strategies such as incorporation of magnetic phases [35] the surface functionalization [36] and stimuli-responsive molecular gates [37] have been also explored for controlled drug delivery purposes. Finally, the processing methods also provide different ways to upgrade the MBGs characteristics. For instance, the MBG preparation as coatings [38] or 3D macroporous scaffolds for bone tissue engineering is also an important ongoing research field. In this sense, macroporous pieces prepared by rapid prototyping techniques [39,40], polymeric templates [41,42,43] or foaming methods [44] have been used by several authors.

Whatever the additives incorporated and/or the processing method used, the synthesis of MBGs requires the addition of a structure directing agent (SDA). In most of the cases, the SDA is an amphiphylic molecule with self-organizing properties at the supramolecular level [45]. The type and amount of SDA

determine the textural properties of MBGs, such as porous structure, pore volume, pore size and also the surface area [46-49]. However, very little is known about the influence of SDA. on the pore wall characteristics such as thickness and local atomic distribution. For instance, the presence of CaP nuclei within silica walls determines the bioactive behavior of MBG, as they determine act as nucleation sites of newly growth apatite [50]. However, these nuclei also entrap the Ca cations avoiding their release to the surrounding media. Finally, the molecular structure of the surfactant determines the pore size and the volume available for the transport of matter between the MBG and the surrounding fluids [51,52]. Despite of this set of evidences, the relationships between the type of SDA,

Materials and methods

Four different MBGs were synthetized by evaporation induced self-assembly (EISA) method. For this aim three different triblock copolymers, Pluronic P123 (EO)20-(PO)70-(EO)20 (Aldrich), F68 (EO)78-(PO)30-(EO)78 and F127 (EO)100-(PO)65-(EO)100 (from BAFS) and a non-ionic alkyl poly(oxyethylene) Brij58 $HO(CH_2CH_2O)_{20}C_{16}H_{33}$ (BASF) were used as structure directing agents. Tetraethyl orthosilicate (TEOS) (98%) Aldrich, triethyl phosphate (TEP) (99%) Aldrich and calcium nitrate $Ca(NO_3)_2 \cdot 4H_2O$ (99%) (Aldrich) were used as SiO_2, P_2O_5 and CaO sources, respectively. In a typical synthesis 2 g of surfactant were dissolved in ethanol with HCl 0,5M solution at room temperature. Afterward TEOS, TEP and $Ca(NO_3)_2 \cdot 4H_2O$ were added under stirring in 3 hours intervals. The different reagents and amounts are shown in table 1. The resulting solution was kept under stirring during 12 hours and cast in Petri dishes (9 cm in diameter). The colorless solution was evaporated at 30ºC for several days (see table 1). Eventually, the dried gels were removed as homogeneous and transparent membranes, and heated at 700ºC for 3 hours under air atmosphere. Finally the MBGs were gently milled and sieved collecting the particle size fraction below 40 μm.

Low angle powder X-ray diffraction experiments were performed with a Philips X'Pert diffractometer equipped with Cu KR radiation (wavelength 1.5406 Å). XRD patterns were collected in the 2θ° range between 0,5θ° and 6,5θ°, with a step size of 0.02θ° and counting time of 4s per step. The textural properties of the calcined materials were determined by nitrogen adsorption porosimetry by using a Micromeritics ASAP 2020 porosimeter. To perform the N_2 adsorption measurements, the samples were previously degassed under vacuum for 15 h, at 150 ºC. The surface area was determined using the Brunauer-Emmett-Teller (BET) method. The pore size distribution between 0.5 and 40 nm was determined from the adsorption branch of the isotherm by means of the Barret-Joyner-Halenda (BJH) method. Transmission electron microscopy (TEM) was carried out with a JEOL-3010 microscope, operating at 300 kV (Cs 0.6 mm, resolution 1.7 Å). Images were recorded using a CCD camera (model Keen view, SIS analyses size 1024 x 1024, pixel size 23.5 mm x 23.5 mm)

mesoporosity, pore wall local structure and bioactivity have been poorly considered.

In this work we have studied the effect of four non-ionic SDAs on the porosity and pore wall characteristics of SiO_2-P_2O_5-CaO MBGs. For the first time, the kind of SDA is used to tailor the properties of multicomponent mesoporous materials, not only at the textural level but also the atomic local environment within the struts of the MBG. These results open the possibility of setting the kinetic of bioactive process and choosing the most appropriated bone graft for each specific patient.

at 30 000x and 60 000x magnification using a low-dose condition. Fourier transform (FT) patterns have been conducted using a digital micrograph (Gatan). $^1H{\rightarrow}^{29}Si$ and $^1H{\rightarrow}^{31}P$ CP (cross-polarization)/MAS (magic-angle-spinning) and single-pulse (SP) solid-state nuclear magnetic resonance (NMR) measurements were performed to evaluate the different silicon and phosphorus environments in the synthesized samples. The NMR spectra were recorded on a Bruker Model Avance 400 spectrometer. Samples were spun at 10 kHz for ^{29}Si and 6 kHz in the case of ^{31}P. Spectrometer frequencies were set to 79.49 and 161.97 MHz for ^{29}Si and ^{31}P, respectively. Chemical shift values were referenced to tetramethylsilane (TMS) and H_3PO_4 for ^{29}Si and ^{31}P, respectively. All spectra were obtained using a proton enhanced CP method, using a contact time of 1 ms. The time period between successive accumulations was 5 and 4 s for ^{29}Si and ^{31}P, respectively, and the number of scans was 10 000 for all spectra. Differential thermal analysis was done a TG/DTA Seiko SSC/5200 thermobalance between 50ºC and 1000ºC at a heating rate of 10ºC·min^{-1}. High resolution scanning electron microscopy was carried out in a field emission JEOL JSM 7600F microscope.

Particle size analysis was carried out by the average grain interception (AGI) method onto the SEM micrographs (ASTM E112). About 100 measurements were made over a set of randomly positioned line segments on the micrographs.

Zeta potential determined by electrophoretic mobility was carried out in a Zetasizer Nano ZS (Malvern Instruments) by suspending MBG particles in phosphate buffered solution at pH 7.4 (PBS).

In vitro bioactivity tests.

Assessments of in vitro bioactivity were carried out on powder samples. For this purpose, 50 mg of powder were soaked into 7 mL of filtered simulated body fluid (SBF) [20], in polyethylene containers at 37 ºC under sterile conditions. The evolution of the glass surface was analyzed by Fourier transform infrared (FTIR) spectroscopy with a Nicolet Magma IR 550 spectrometer and by scanning electron microscopy (SEM) using a JEOL F-6335 microscope. Finally, MBGs dissolution tests were made by measuring the Ca^{2+} concentration as a function of soaking time in SBF with an Ilyte system.

Table 1. Nominal composition, surfactant and synthesis conditions for the different mesoporous bioactive glasses

Sample	Nominal composition (% mol)	TEOS (g)	TEP (g)	Ca(NO$_3$)$_2$ (g)	Ethanol (g)	HCl (mL)	Gelling (days)
85S-Brij58	SiO$_2$ 85-CaO 10-P$_2$O$_5$ 5	3.70	0.34	0.49	30	0.8	7
85S-F68	SiO$_2$ 85-CaO 10-P$_2$O$_5$ 5	3.70	0.34	0.49	30	0.5	11
85S-P123	SiO$_2$ 85-CaO 10-P$_2$O$_5$ 5	3.70	0.34	0.49	30	0.5	6
85S-F127	SiO$_2$ 85-CaO 10-P$_2$O$_5$ 5	3.70	0.34	0.49	40	1	8

Cell culture.

Murine MC3T3-E1 preosteoblasts (as undifferentiated osteoblast-like cells) were seeded on well culture plates (CULTEK), at a density of 105 cell/mL in Dulbecco's Modified Eagle's Medium (DMEM, Sigma Chemical Company, St. Louis, MO, USA) with 10% fetal bovine serum (FBS, Gibco, BRL), 1 mM L-glutamine (BioWhittaker Europe, Belgium), penicillin (200 mg·mL-1, BioWhittaker Europe, Belgium), and streptomycin (200 mg·mL-1, BioWhittaker Europe, Belgium), under a CO2 (5%) atmosphere at 37 ℃ for 24 hours to reach the confluence in each cell plate. After that the MBG powders, previously sterilized at dried heat at 150ºC during 24 hours, were added on the seed cells at confluence at 1mg/mL of concentration.

Mitochondrial activity. In order to evaluate the cell mitochondrial activity of living cells in contact with the MBGs for 1 and 7 days of incubation, MTT method was employed based on the reduction of yellow 3[4,5-dimethylthiazol-2yl]-2,5-diphenyltetrazolium bromide to blue formazan. For this aim, the culture media were replaced with 1 mL of DMEM and 125 μL of 0.012 g L^{-1} MTT solution in PBS. Samples were incubated for 4 h at 37 ℃ and 5% CO$_2$ under dark conditions. Then, the medium was removed and 500 μL of 0.4N isopropanol–HCl were added. Finally, the absorbance was measured at 570 nm using a Helios Zeta UV-VIS spectrophotometer.

Alkaline phosphatase activity. The alkaline phosphatase (ALP) activity of cells growing in presence of MBG powders was used as the key differentiation marker in assessing expression of the osteoblast phenotype. ALP activity was measured on the basis of the hydrolysis of p-nitrophenylphosphate to p-nitrophenol. For this purpose, MC3T3 cells were seeded in the same conditions but using supplemented medium with b-glycerolphosphate (50 mg mL-1, Sigma Chemical Company, St. Louis, MO, USA) and L-ascorbic acid (10 mM, Sigma Chemical Company, St. Louis, MO, USA). Moreover, the total protein value after 10 days was determined by a colorimetric method at 540 nm (Bio-Analítica, S.L.), using a Helios Zeta UV-VIS spectrophotometer.

Statistics

Data are expressed as means ± standard deviations of three experiments. Statistical analysis was performed using the Statistical Package for the Social Sciences (SPSS) version 11.5 software. Statistical comparisons were made by analysis of variance (ANOVA). Subsequently, post hoc analyses were carried out to correct for multiple comparisons.

Results and discussion

Table 2 show the zeta potential measurements and particle size for the four MBGs prepared. The results indicate that the use of the different SDA does not affect the surface charge or the particle size. Surface charge is determined by the chemical composition of the materials, mainly SiO$_2$, which shows negative potential values at pH 7.4. Besides, the similar particle sizes for the four MBGs indicate that the milling and sieving process determine this parameter independently of the SDA used.

Table 2. Zeta potential and particle size measured for the four MBGs prepared. Values in brackets indicate the standard deviation)

Sample	Zeta potential (mV)	Particle size (μm)
85S-Brij58	-15.9	18 (±10)
85S-F68	-12.1	32 (±16)
85S-P123	-15.6	26 (±14)
85S-F127	-16.1	23 (±15)

Figure 1 shows the low-angle XRD patterns of the four MBGs synthetized. XDR pattern for 85S-Brij58 does not show any diffraction maxima pointing out the disordered structure of this material. 85S-F68 and 85S-P123 show a single peak at 1.38° and 1.26° 2θ°, respectively. This maximum could correspond to the (10) reflexion of a 2D hexagonal p6m structure based on TEM results (see below). 85S-F127 presents an intense maximum at 0.94° 2θ and two less intense peaks at 1.64° and 1.88° 2θ, which could be assigned to the (10), (11) and (20) reflections, respectively, of 2D hexagonal p6m structure. The structural data calculated by XRD experiments are shown in table 3.
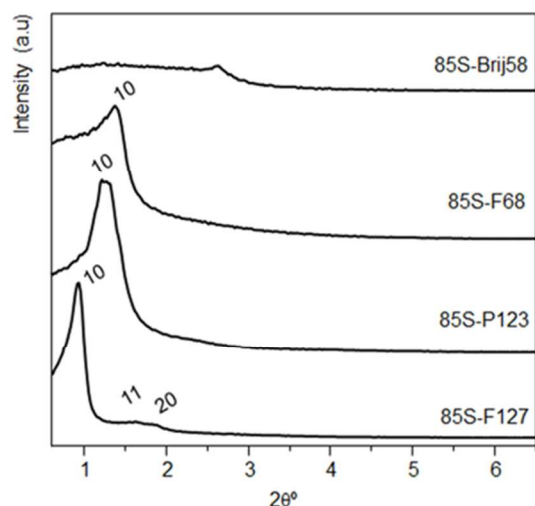
Figure 1. Low angle XRD patterns of the mesoporous 85SiO$_2$-10CaO-5P$_2$O$_5$ glasses synthetized with different structure directing agents.

Table 3. XRD results obtained for the four MBGs prepared

Sample	2Theta	d$_{hkl}$ (nm)	hkl	a$_0$ (nm)
85S-Brij58	NA	NA	NA	NA
85S-F68	1.38	6.41	10 (p6m)	7.40
85S-P123	*1.26*	*7.05*	*10 (p6m)*	*8.14*
85S-F127	0.94	9.46	10 (p6m)	10.90
	1.64	5.45	11 (p6m)	
	1.88	4.78	20 (p6m)	

Figure 2 shows the TEM images and FT patterns for the 85S-MBGs prepared with the four different SDAs. TEM images evidence differences in the mesoporous ordering as a function of the SDA used. The HRTEM images for 85S-Brij58 (figure 2a and 2b) evidence a disordered porous material as confirmed by the absence of maxima in the FT pattern and in agreement with the absence of diffraction maxima in the XRD pattern. HRTEM images of 85S-P123 (figure 2c and 2d) indicate a 2D-hexagonal mesoporous structure coexisting with a disordered worm-like porous phase. Finally, TEM images for 85S-F68 (figure 2e and 2f) and 85S-F127 (figure 2g and 2h) clearly correspond to a 2D hexagonal symmetry with a p6m planar group, thus confirming the results obtained by XRD.

Figure 3 shows the N$_2$ adsorption isotherms and pore size distribution for the four materials synthetized. 85S-Brij58 shows a type I isotherm characteristic of microporous materials. The pore size distribution indicates a monomodal distribution centered at the micropore range (1.87nm) with an asymmetric tail towards the mesopore region. 85S-F68, 85S-P123 and 85S-F127 materials exhibit type IV isotherms characteristic of mesoporous materials. Whereas 85S-P123 and 85S-F127 isotherms show H1-type hysteresis loops associated to

cylindrical pores opened at the ends, 85S-F68 exhibits a H2-type loop characteristic of ink-bottle pore or cylindrical pores with narrowings along the channels. Pore size distributions show porosities at the mesopore ranges (over 2 nm) with different pore sizes depending on the triblock copolymer used.
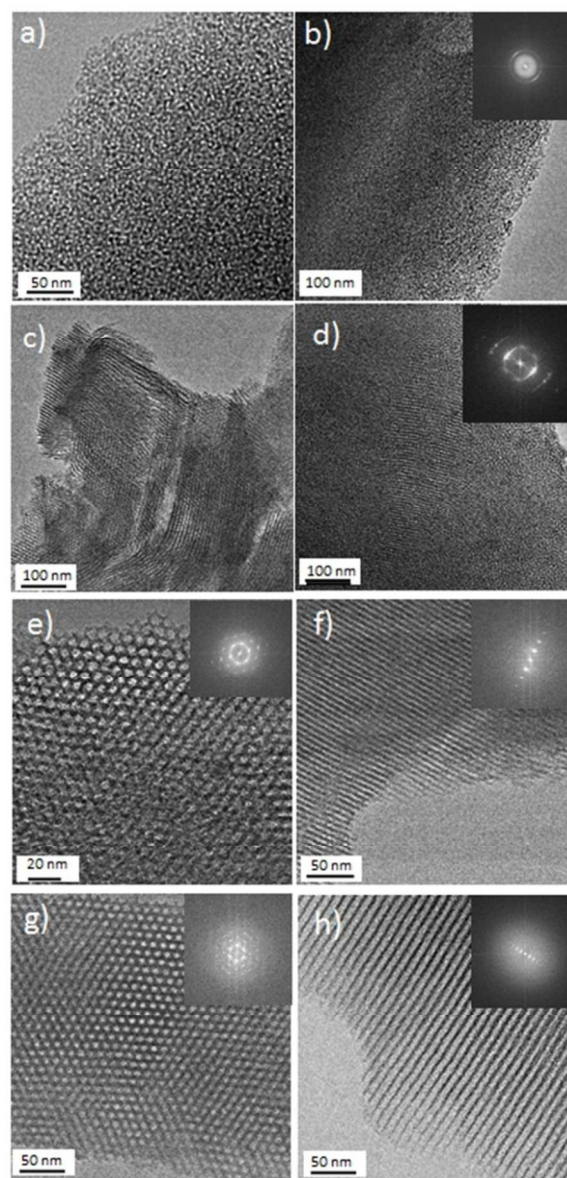

Figure 2. HRTEM images and FT diagrams obtained from 85S-Brij58 (a and b), 85S-P123 (c and d), 85S-F68 (e and f) and 85S-F127 (g and h)

The textural parameters are summarized in table 4. Samples prepared with triblock copolymers (i.e. F68, P123 and F127) show S$_{BET}$ and pore volume values in the range of MBGs [1,2,13]. 85S-Brij58 exhibits the highest S$_{BET}$ and pore volume compared with the others materials. This fact indicates that, despite of the disordered structure evidenced by XDR and TEM, Brij58 interacts with the inorganic phase thus raising a microporous material with high textural values. The pore sizes keep relation with the lengths of the hydrophobic chains of the surfactants, i.e. the poly-propylene oxide (PO)n block. Thus

P123 and F127 (with 70 and 65 units of (PO), respectively) lead to pore sizes significantly larger than F68 (with 30 units of PO) and Brij 58 (with a hydrophobic block composed of a $-C_{16}H_{33}$ hydrocarbide chain).
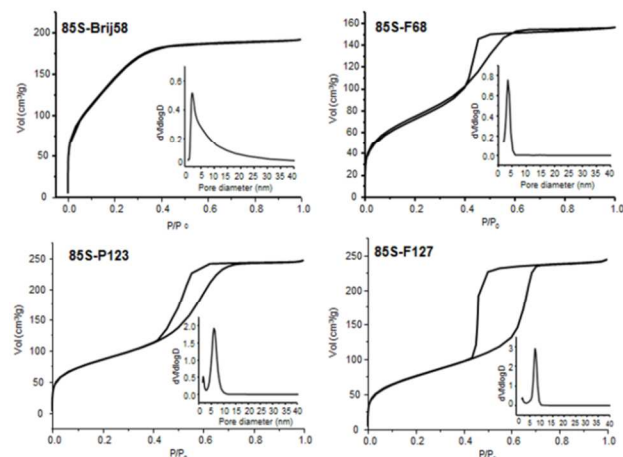

Figure 3. N_2 adsorption isotherms of $85SiO_2$-$10CaO$-$5P_2O_5$ glasses synthetized with different structure directing agents. The insets show the pore size distributions

Wall thicknesses were calculated from the lattice parameter a (obtained by XRD) and the pore sizes (obtained by the BJH method). The wall thickness can be related with the size of the hydrophilic chains of the triblock copolymer. F68 and F127 with longer the EO chains (78 and 100 EO units, respectively) lead to thicker walls than P123 (with hydrophilic chains of 20 EO units). In the case of 85S-Brij58 this parameter could not be calculated due to the disordered structure of this material.

Table 4. Textural parameters obtained by N_2 adsorption porosimetry for ordered MBGs

Sample	S_{BET} (m^2g^{-1})	Pore Size (nm)	Pore volume (cm^3/g)	a_0 (nm)	Wall Thick. (nm)
85S-Brij58	572.1	1.87	0.44	NA	NA
85S-F68	261.3	3.36	0.38	7.40	3.05
85S-P123	310.7	5.92	0.37	8.14	2.22
85S-F127	269.6	7.18	0.29	10.90	3.72

^{31}P-NMR results were used to evaluate the local environment of P atoms, thus elucidating the phosphate species contained in the different samples (Figure 4). The spectra recorded by single pulse show one signal at ~2 ppm assignable to q0 units present in the PO_4^{3-} species. The signals show a full width at half-maximum height (fwhm) of around 7 ppm, which is typical of

an amorphous orthophosphate [25]. These results evidence that most of the P atoms are included as independent PO_4^{3-} tetrahedrons within the silica network. The orthophosphates would be balanced with the Ca^{2+} cations introduced in the system, thus resulting in amorphous calcium orthophosphate. This fact would avoid the polyphosphate formation, independently of SDA used. $^1H{\rightarrow}^{31}P$-CP spectra were collected to study the local environment of the P atoms in those regions close to the Si-OH groups, i.e. the material surface. $^1H{\rightarrow}^{31}P$-CP spectra evidence the same situation, pointing out that the phosphate groups are orthophosphates in both the surfaces and the inner locations of the MBG walls.

Table 5 shows the chemical shifts, deconvoluted peak areas, and silica network connectivity of MBG85 for each SDA incorporated to the synthesis. Single pulse ^{29}Si MAS NMR spectra evidence significant differences in the network connectivity (NC), which are dependent on the SDA used. Interestingly, the NC increases with the SDA as follows: Brij-58<F68<P123<F127, which is the same trend observed for the pore size. The NC in SiO_2-P_2O_5-CaO bioactive glasses has been commonly related to the amount of Ca^{2+} cations within the SiO_2 network, not with the pore size [50]. In fact, Ca^{2+} acts as network modifiers reducing the amount of Q^4 units and increasing the glass bioactivity. Since the four MBGs synthesized in this work contains the same amount of Ca^{2+}, the different network connectivity must be explained in terms of a different distribution of Ca^{2+} cations within the silica network.
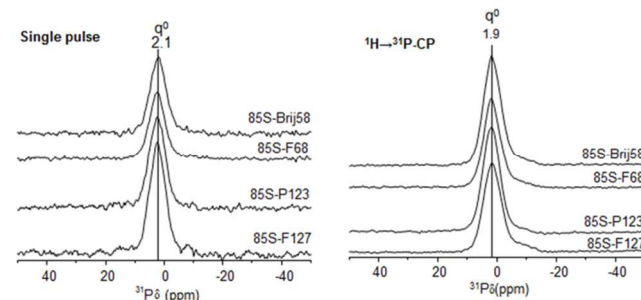

Figure 4. Solid-state ^{31}P single-pulse (top) and cross-polarization (bottom) MAS NMR spectra of the $85SiO_2$-$10CaO$-$5P_2O_5$ bioglasses synthetized with different structure directing agents

Journal Name

RSCPublishing

ARTICLE

Table 5. Chemical shift, relative peaks areas and silica connectivity obtained by solid-state single pulse ^{29}Si MAS NMR

	Q^2		Q^3		Q^4		
Sample	Chemical shift	Relative peak area	Chemical shift	Relative peak area	Chemical shift	Relative peak area	Network connectivity
85S-Brij58	-93.11	3.9	-101.3	20	-110.87	76.1	3.72
85S-F68	-92.73	0,93	-101.24	18.8	-111.3	80.2	3.79
85S-P123	-94.93	3	-101.4	13.8	-111.1	83.2	3.80
85S-F127	-93.8	2	-101.9	13	-110.9	85	3.96

SiO_2-P_2O_5-CaO MBGs contain Ca^{2+} cations in two different local environments; i) taking part of calcium orthophosphate heterogeneities segregated out of the silica network and ii) dispersed within silica network (and mainly placed at the wall surface) thus acting as network modifiers [53]. This Ca^{2+} distribution has been previously observed [8,25,50] and it is in clear agreement with the NMR studies presented in this work. In our case, the composition $85SiO_2$-$5P_2O_5$-$10CaO$ has a theoretical NC = 3.69, considering SiO_2 and P_2O_5 as network formers and CaO as network modifiers. The NC calculated for our four MBGs (table 4) are higher, indicating that Ca^{2+} are partially sequestered into CaP heterogeneities and the SiO_2 network is thus depleted of network modifiers. There are also clear differences of NC between the MBGs. 85S-Brij58 has a NC very similar to the theoretical one (3.72 vs 3.69), pointing out that most of Ca^{2+} are acting as network modifier in this MBG and only a little amount of Ca^{2+} is sequestered as CaP clusters. However the NC for 85S-F127, i.e. 3.96) clearly indicates that most of Ca^{2+} is taken out of the SiO_2 network. Even more interesting, there is a clear correlation between the network connectivity and the pore size (see table 3). This fact seems to indicate that formation of CaP heterogeneities is easier when the pore diameter is larger, perhaps because the nucleation of CaP clusters is also affected by steric factors.

The higher or lower presence of CaP heterogeneities is assessed by analyzing the vitreous transition temperature (Tg). DTA experiments (table 6) show that Tg correlates with the presence of CaP heterogeneities, i.e. the moretheCaP nuclei the lower the T_g, following the trend F127 < P123 < F68 < Brij-58. This behavior can be explained in terms of CaP heterogeneities acting as microstructural defects, which would decrease the T_g.

In vitro bioactivity tests

In vitro bioactivity tests were carried out by soaking powdered MBGs in SBF and studying the changes occurred onto the MBGs surfaces. FTIR spectroscopy was carried out to evaluate the changes in the bioglasss surface as a function of soaking time. The powders were soaked in SBF for different times.

Table 6. Glass transition temperature and mass loss results obtained by TG/ATD.

Sample	Glass transition temperature (ºC)
85S-Brij58	846.13
85S-F68	829.90
85S-P123	811.16
85S-F127	784.40

Figure 6 shows the FTIR spectra obtained after 0, 1, 6 and 24 hour in contact with SBF. Before soaking, the four MBGs show almost identical spectra, with the characteristic absorption bands of Si-O bonds at approximately 1040 cm^{-1} (Si-O-Si stretching), 800 cm^{-1} (Si-O-Si rocking) and 470 cm^{-1} (Si-O-Si bending). After one hour in contact with SBF, a singlet absorption band at 600 cm^{-1} can be observed in the four MBGs. This band correspond to the bending mode O-P-O characteristic of phosphate in amorphous environment, which is a normal stage during the bioactive processes occurred onto bioactive glasses when they are soaked into biomimetic solutions [7]. After 6 six hours in contact with SBF, 85S-Brij58, 85S-P123 and 85S-F127 (figures 6a, 6c and 6d) still show the same singlet band at 600 cm-1 corresponding to
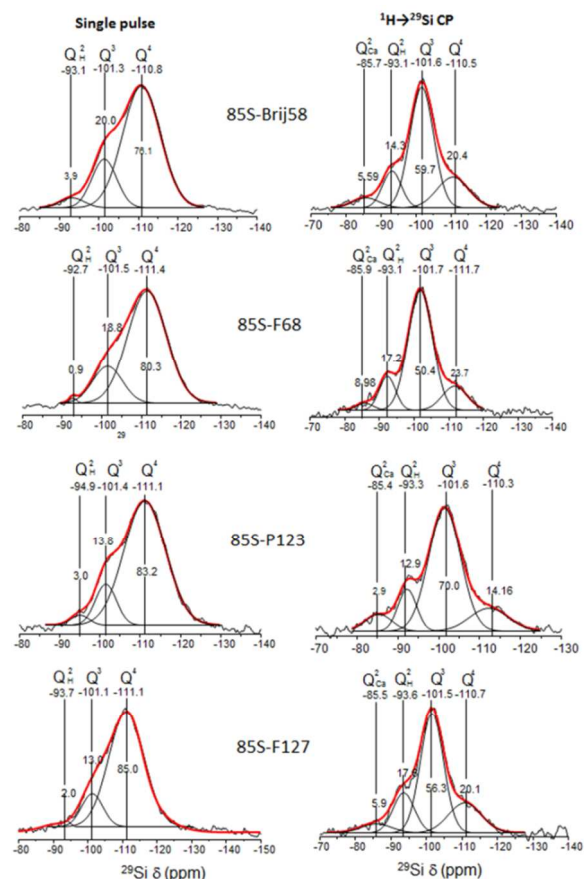
Figure 5. Solid-state ^{29}Si single-pulse (left) and cross-polarization (right) MAS NMR spectra of the four mesoporous 85SiO$_2$-10CaO-5P$_2$O$_5$ glasses samples. The areas for the Q^n units were calculated by Gaussian line-shape deconvolutions and are displayed by grey dotted lines (their relative populations are expressed as percentages)

Figure 6. FTIR spectra as a function of soaking time in SBF for 85S-Brij58 (a), 85S-F68 (b), 85S-P123 (c) and 85S-F127 (d)

amorphous phosphate. On the contrary, in the case of 85S-F68 this signal appears as a doublet at 580-610 cm^{-1} corresponding to the bending mode of O-P-O in a crystalline environment. In S85-F68 MBG, the amorphous CaP turns faster into crystalline apatite compared to any other MBG studied in this work. After 24 hour, all the samples have developed an apatite like phase onto the surfaces, as can be deduced from the doublet a 580-610 cm^{-1}. However, from a semiquantitative point of view, the intensity of this signal is higher in 85S-F68 when compared with any other, especially with 85S-F127.

In order to confirm these results, the samples surfaces were observed by SEM after 0, 6 and 24 hours in contact with SFB and the micrographs are shown in Figure 7. The insets indicate the Ca/Si ratio measured by EDX and provide an estimation of
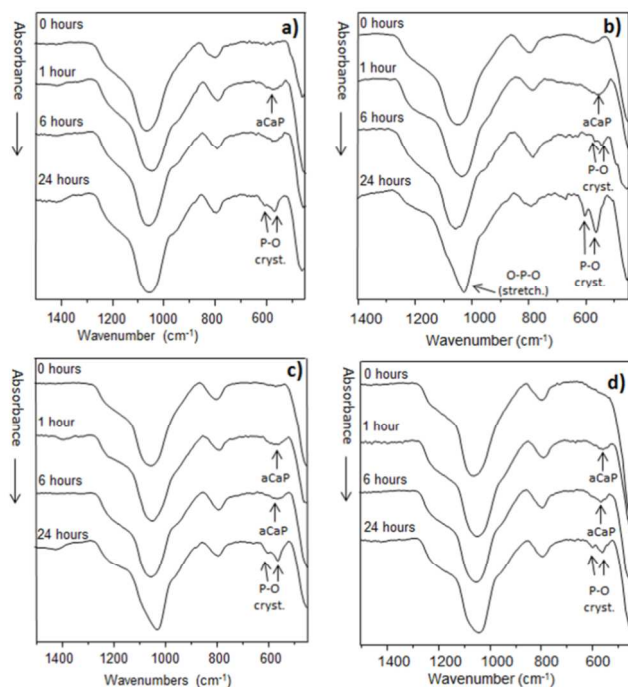
the bioactive process stage, considering Ca dissolution from the MBG to SBF, or Ca precipitation as hydroxyapatite from SBF onto MBG.

Before soaking in SBF the MBGs grains show smooth surfaces, with some particles smaller than 1 micrometer attached to them. The EDX analyses indicate a Ca/Si ratio close to the theoretical one (0.12). After 6 hours in SBF, the surface of 85S-Brij58 appears covered by aggregates of rounded particles, indicating that a new phase has grown on it. The Ca/Si ratio is similar to the glass before soaking. However, considering that Ca is
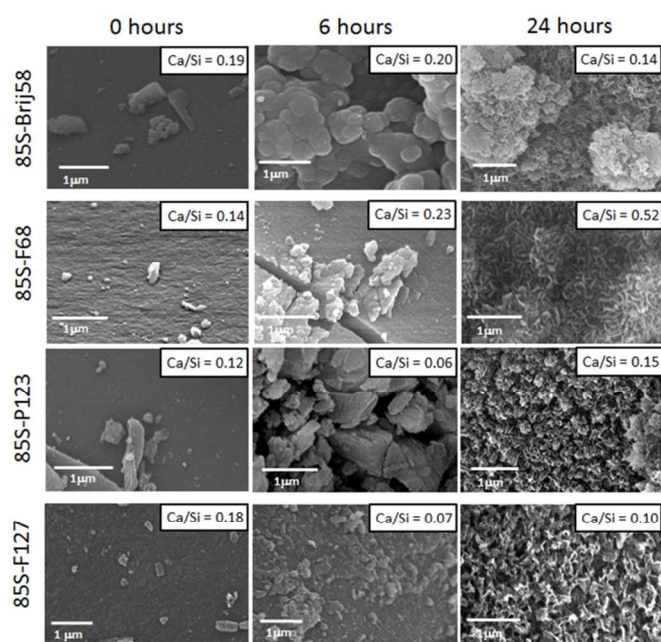
Figure 7. SEM micrographs of the 85SiO2-10CaO-5P2O5 glasses synthetized with different structure directing agents, after being soaked in SBF for 0, 6 and 24 hours. The Ca amounts at the surface measured by EDX spectroscopy is pointed into an inset for each micrograph.

initially released during the first stages of the bioactive process [7,14,21], the similar Ca/Si ratio would indicate that the precipitation of Ca as calcium phosphate have also occurred, thus explaining the new phase appeared in the micrograph. In the case of 85S-F68, the precipitation of a new phase after 6 hours is even more intense. The micrograph shows a thick and dense newly formed phase that has precipitated onto the surface. This phase cracks under the electron beam as can be appreciated in the micrograph, which is very common in newly formed apatite phases when observed by SEM at high magnification. The EDX analysis confirm that, after the initial calcium release, the surface contains more calcium than before soaking and confirms the precipitation of a large amount new calcium phosphate onto the surface of 85S-F68 glass. The surfaces of MBGs 85S-P123 and 85S-F127 appear with an increase of porosity. The pinholes would indicate that a dissolution process prevail over the precipitation one. This observation agrees with the decrease of Ca/Si ratio observed by EDX, which point out that the amount of amorphous calcium phosphate precipitated does not compensate the Ca dissolution occurred during the first hours of the bioactive process. Finally, after 24 hours the formation of an apatite-like phase is evidenced over the surface of the four MBGs studied in this work. However, from a quantitative point of view, the amount of apatite grown onto 85S-F68 is significantly larger as can be observed from the Ca/Si ratio and agreeing with the FTIR results.

Figure 8 shows the HR-TEM images of 85S-F68 and 85S-F127 after 6 hours in contact with SBF. The image obtained for MBG 85S-F68 (figure 8a) shows the formation of a crystalline phase (signed as HA). The EDX analysis made during the observation (data not shown) confirmed that these crystals are a calcium phosphate phase. In order to study the structure of this new formed CaP, higher magnification and electron diffraction experiment were carried out (figure 8b). The ED pattern (inset in figure 8b) demonstrates that the newly formed calcium phosphate phase is an apatite like phase, in agreement with the FTIR results. On the contrary, 85S-F127 after 6 hours (figures 8c and 8d) in contact with SBF does not show the formation of this apatite phase, also confirming the FTIR data.

The kinetic of HA formation onto the MBGs surface indicates that 85S-F68 is fastest material in developing a new apatite phase under in vitro conditions, among the MBGs studied in this work. 85S-F68 exhibits the smallest pore size among the MBGs with a 2D-hexagonal p6m structure (85S-Brij58 shows a pore size even smaller but this glass does not exhibit mesoporous ordering). The structural studies of the MBGs indicated that the presence of CaP heterogeneities in 85S-F68 is lesser compared with 85S-P123 and 85S-F127. Consequently, 85S-F68 contains more free Ca^{2+} cations as network modifiers to exchange with protons of SBF and, in this way, initiate the bioactive process faster. In the opposite way, 85S-F127 with larger pore sizes, the formation of CaP clusters is facilitated. In fact, the high connectivity of the silica network (3.96) indicates that the amount of network modifiers Ca^{2+} cations is very low. Consequently, the Ca^{2+} dissolution and subsequent hydroxyapatite growth seems to be slowed. This point is confirmed by the measurement of Ca^{2+} dissolution in SBF as a function of soaking time (Figure 9). The calcium release profiles show that the four MBGs prepared release calcium to the surrounding fluid during the first hour, due to the initial dissolution of the MBS in a hydric medium. Thereafter the calcium concentrations decrease, which is in agreement with the new calcium phosphate growth as evidenced by FTIR and SEM. The different dissolution degrees also keep a close relationship with the local environment of the MBGs determined by NMR. 85S-F68 and 85S-Brij58 exhibit the largest dissolution processes whereas 85S-F127 is significantly less soluble than the rest of the MBGs. This behavior would confirm the NMR results, which indicate the higher amount of Ca^{2+} acting as network modifier in 85S-F68 and 85S-Brij58 compared with 85S-F127.

In order to study the influence of the different MBGs over bone cells, preliminary cell culture tests with pre-osteoblasts were carried out in the presence of the four prepared materials. Figure 10.a shows the mithocondrial activity of pre-osteoblast after 1 day of exposure to the different MBGs. Pre-osteoblast showed a good proliferative behavior without significant differences among them. In order to study the osteoinductive capability of the different MBGs, ALP contents were measured as an osteoblast differentiation (figure 10 b). After 10 days in contact, significant differences could be observed between 85S-F68 and 85S-F127, pointing out that the differentiation from

pre-osteoblast towards osteoblast phenotype is higher in the case of 85S-F68. This result could be related with the larger Ca^{2+} release and better bioactive behavior shown by this MBG, although further studies are required to confirm this point.
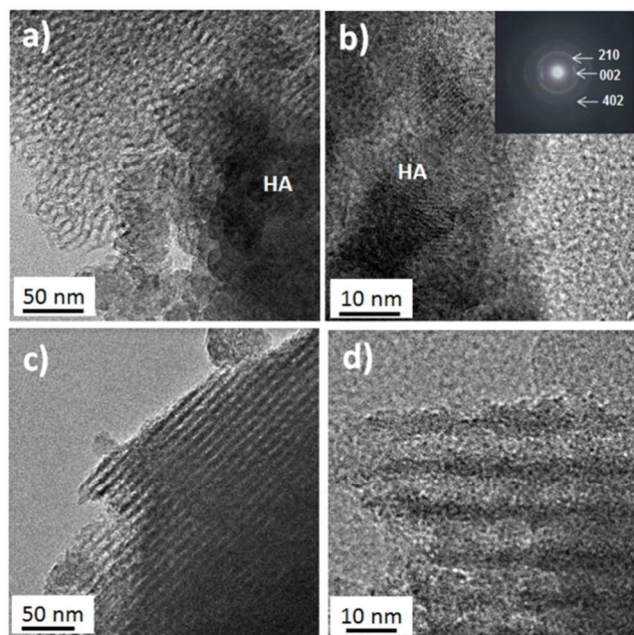

Figure 8. (a) HR-TEM image of 85S-F68 MBG after 6 hours soaked in SBF; HA indicates a calcium phosphate crystals observed in this sample; (b) Higher magnification of image (a). The inset show the ED pattern obtained from the area pointed as HA. (c) and (d) HR-TEM images of 85S-F127MBG after 6 hours soaked in SBF.

In addition to the Ca^{2+} local environment, the mesoporous ordering facilitates the bioactive process. In this sense, 85S-F68 is more bioactive than 85S-Brij58, although the latest contains more Ca^{2+} cations as network modifiers. However, the very small pore size of 85S-Brij58 (1.87 nm, i.e. below the mesopore range) and the tortuosity of its worm-like structure seems not to favor the HA nucleation and growth when compared with 85S-F68.
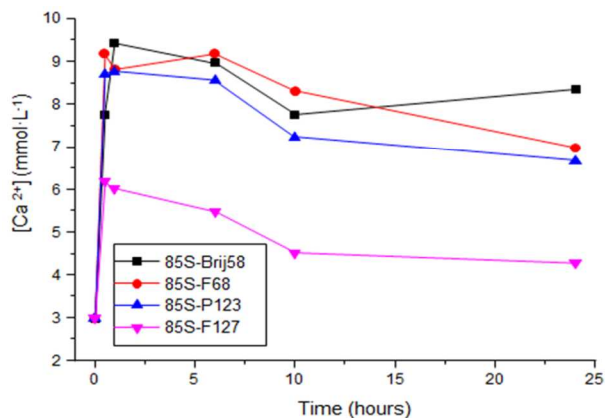

Figure 9. Ca2+ release as a function of soaking time for the four MBGs synthesized
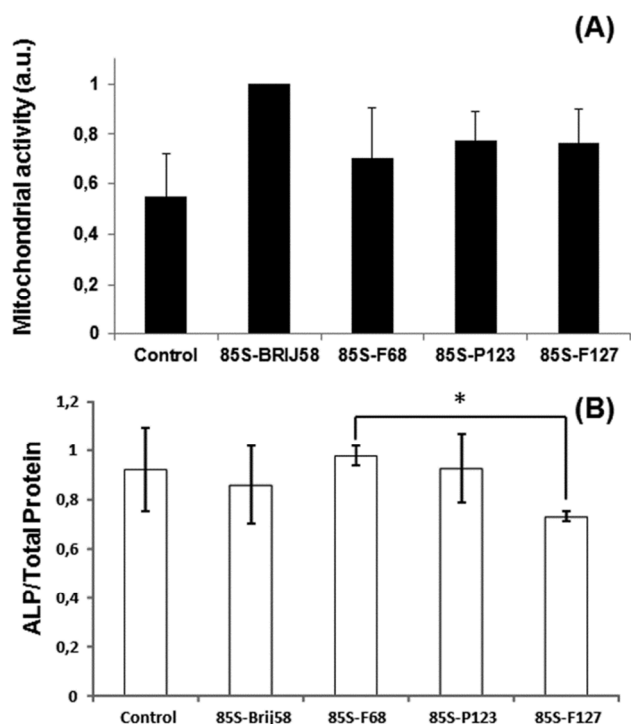

Figure 10. (a) Mitochondrial activity of preosteoblast MC3T3 cells in presence of 1mg/ml of MBG in powder after 1 day of incubation. (b) ALP per total protein of preosteoblast MC3T3 cells in presence of different MBG powder after 10 days of incubation. The controls correspond to MC3T3 cells incubated in the absence of MBG powder. (*) Significant differences between 85S-F68 and 85S-F127 (P<0.05) are shown.

The accessibility of the pores to the surface is also a very important factor. We wondered if the lower bioactivity of 85S-F127 could be due to the non- accessibility of the open pores to the surface. In order to assess the pore accessibility of this MBG, we carried out high resolution scanning electron microscopy (HR-SEM). The micrograph obtained with this powerful tool is shown in Figure 10, and evidences an opened porosity accessible to the external surface.
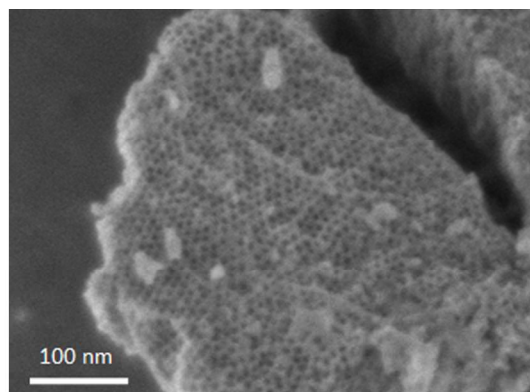

Figure 11. HR-SEM micrographs of 85S-F127 evidencing the 2D-hexagonal mesoporous structure opened to the external surface

Finally, we want to highlight the interesting point of view of Deng et al about the possible block of the porous system during the bioactive process [54]. These authors demonstrated that the CaP nuclei formed during the first stages of the bioactive process can obstruct the mesoporous structure if they have enough space to nucleate within the mesopores. This fact results in a delaying of the newly apatite layer formation, as the ionic exchange from the inner regions of the MBG is impeded. These authors reported that the critical nucleation diameter 2r* for HA is above 2.7 nm and below 4.9 nm. These studies agree with our results, indicating that 85S-F127 and 85S-P123 with pore sizes of 5.92 nm and 7.18 nm, respectively, would form these stoppers that partially avoid the matter exchange with SBF. On the contrary, 85S-F68 with pore size of 3.36 does not undergo this impediment. These results open new perspectives to tailor mesoporous materials based in multicomponent systems for different applications. In the specific case of bone regeneration purposes, the capability of designing the porous structure and the atomic environment can determine the success or failure in restoring the life quality of the patients.

Conclusions

Microporous and mesoporous bioactive glasses, in the system $85SiO_2-10CaO-5P_2O_5$, have been prepared with different structure directing agents. The glasses thus prepared range from microporous disordered structures to ordered mesoporous arrangements.

By choosing the appropriated structure directing agent we can tailor the pore size and the wall thickness for a specific MBG composition.

The local distribution of Ca cations and CaP heterogeneities formation is dependent on the SDA used. Those SDAs leading to larger pore sizes facilitate the formation CaP heterogeneities, increases the slica network connectivity and result in MBGs with slower bioactive behaviors.

MBGs with ordered mesoporous structure and smaller pore size exhibit faster in vitro bioactive behavior. Specifically, MBG prepared with F68 triblock copolymer contains less CaP heterogeneities and more Ca^{2+} cations available for ionic exchange. In addition, its small diameter would impede the newly formed CaP nuclei within the pores during the bioactive process, which could obstruct the matter transfer between the glass and the surrounding media.

Preliminary pre-osteoblast culture tests indicate that the four MBGs are biocompatible without significant differences respect to the proliferative behavior of the cells. However, the MBGs prepared with F68 as SDA induces the differentiation toward osteoblast phenotype in a faster way than the MBG prepared with F127.

These findings demonstrate the significance of the local atomic environment and the pore size beyond the chemical composition and surface area, which are classically considered as the most significant parameters involved in the in vitro bioactivity and cell response.

Notes and references

[a] Departamento de Química Inorgánica y Bioinorgánica. Facultad de Farmacia, Universidad Complutense de Madrid. Instituto de Investigación Sanitaria Hospital 12 de Octubre i+12. Plaza Ramón y Cajal s/n, 28040 Madrid, Spain.

[b] CIBER de Bioingeniería, Biomateriales y Nanomedicina (CIBER-BBN), Spain.

*Corresponding authors e-mail: arcosd@ucm.es; vallet@ucm.es.

1. C. Wu, J. Chang. *Interface Focus*. 2012, **2**, 292.
2. D. Arcos, M. Vallet-Regí. *Acta Biomater*. 2010, **6**, 2874.
3. L.L. Hench, J.M. Polack. *Science* 2002, **295**, 1014.
4. M. Vallet-Regí. *Dalton Trans* 2006, **44**, 5211.
5. T. Kresge, M.E. Leonowicz, W.J. Roth, J.C. Vartuli, J.S. Beck. *Nature* 1992, **359**, 710.
6. D. Zhao, J. Feng, Q. Huo, N. Melosh, G.H. Fredrickson, B.G. Chmelka, G.D. Stucky. *Science* 1998, **279**, 548.
7. I. Izquierdo-Barba, D. Arcos, Y. Sakamoto, O. Terasaki, A. López-Noriega, M. Vallet-Regí. *Chem Mater*. 2008, **20**, 3191.
8. P.N. Gunawidjaja, A.Y.H. Lo, I. Izquierdo-Barba, A. García, D. Arcos, B. Stevensson, M. Vallet-Regí, M. Eden. *J. Phys. Chem. C* 2010, **114**, 19345.
9. M. Vallet-Regí, F. Balas, D. Arcos. *Angew. Chem. Int. Ed*. 2007, **46**, 7548.
10. D. Arcos, A. López-Noriega, E. Ruiz-Hernández, O. Terasaki, M. Vallet-Regí. *Chem. Mater*. 2009, **21**, 1000.
11. C. Wu, J. Chang. *J. Control Release*. 2014, **193**, 282.
12. D. Arcos, M. Vallet-Regí. M. *Acta Mater*. 2013, **61**, 890.
13. X. Yan, C. Yu, X. Zhou, J. Tang, D. Zhao. *Angew. Chem. Int. Ed.* 2004, **43**, 5980.
14. R. Li, A.E. Clark, L.L. Hench. *J. Appl. Biomater*. 1991, **2**, 231.
15. J. Zhong, D.C. Greenspan. *J. Biomed. Mater. Res*. 2000, **53**, 694.
16. M. Hamadouche, A. Meunier, D.C. Greenspan, C. Blanchat, J.P. Zhong, G.P. La Torre, L. Sedel. *J. Biomed. Mater. Res.* 2001, **54**, 560.
17. M. Vallet-Regí, C.V. Ragel, A.J. Salinas. *Eur. J. Inorg. Chem.* 2003, 1029.
18. D. Arcos, D.C. Greenspan, M. Vallet-Regí. *Chem. Mater.* 2002, **14**, 1515.
19. M. Vallet-Regí, A.J. Salinas, D. Arcos. *J. Mater. Sci: Mater. Med.* 2006, **17**, 1011.
20. T. Kokubo, H. Kushitani, S. Saka, T. Kitsugi, T. Yamamuro. *J. Biomed. Mater. Res.* 1990, **24**, 721.
21. L.L. Hench. *J. Am. Ceram. Soc.* 1991, **74**, 1487.
22. T. Kokubo, H. Takadama. *Biomaterials* 2006, **27**, 2907.
23. M. Bohner, J. Lemaitre. *Biomaterials* 2009, **30**, 2175.

24. X. Yan, X. Huang, C. Yu, H. Deng, Y. Wang, Z. Zhang. *Biomaterials* 2006, **27**, 3396.

25. E. Leonova, I. Izquierdo-Barba, D. Arcos, A. Lopez-Noriega, N. Hedin, M. Vallet-Regí, M. Eden. *J Phys Chem C* 2012, **112**, 5552.

26. M. Alcaide, P. Portoles, A. López-Noriega, D. Arcos, M. Vallet-Regí, M.T. Portoles. *Acta Biomater*. 2010, **6**, 892.

27. X. Li, X.P. Wang, D.N. He, J.L. Shi. *J. Mater. Chem.* 2008, **18**, 4103.

28. C. Wu, W. Fan, M. Gelinsky, Y. Xiao, P. Simon, R. Schulze, T. Doert, Y. Luo, G. Cuniberti. *Acta Biomater.* 2011, **7**, 1797.

29. C. Wu, Y. Zhou, C. Lin, J. Chang, Y. Xiao. *Acta Biomater.* 2012, **8**, 3805.

30. C. Wu, R. Miron, A. Sculean, S. Kaskel, T. Doert, R. Schulze, Y. Zhang. *Acta Biomater.* 2011, **32**, 7068.

31. C. Wu, Y. Zhou, W. Fan, P. Han, J. Chang, J. Yuen, M. Zhang, Y. Xiao. *Biomaterials* 2012, **33**, 2076.

32. C. Wu, Y. Zhou, M. Xu, P. Han, L. Chen, J. Chang, Y. Xiao. *Biomaterials* 2013**, 34**, 422.

33. A.J. Salinas, S. Shruti, G. Malavasi, L. Menabue, M. Vallet-Regí. *Acta Biomater.* 2011, **7**, 3452.

34. S. Shruti, A.J. Salinas, G. Lusvardi, G. Malavasi, L. Menabue, M. Vallet-Regí. *Acta Biomater.* 2013, **9**, 4836.

35. X. Li , X. Wang , Z. Hua , J. Shi. *Acta Materialia*, 2008, **56**, 3260.

36. A. López-Noriega, D. Arcos, M. Vallet-Regí. *Chem. Eur. J.* 2010, **16**, 10879.

37. H.M Lin, W.K. Wang, P.A. Hsiung, S.G. Shyu. *Acta Biomater.* **2010**, *6*, 3256.

38. X. Wang, X. Li, K. Onuma, A. Ito, Y. Sogo, K. Kosuge, A. Oyane. *J. Mater. Chem,* 2010, **20**, 6437.

39. H.S. Yun, S.E. Kim, Y.T. Hyeon. *Chem. Comm* 2007, 2139.

40. H.S. Yun, S.E. Kim, Y.T. Hyeon, S.J. Heo, J.W. Shin. *Chem. Mater.* 2007, **19**, 6363.

41. G.F. Wei, X.X. Yan, J. Yi, L.Z. Zhao, L. Zhou, Y.H. Wang, C.Z. Yu. *Microporous Mesoporous Mater* 2011, **143**, 157.

42. Y.F. Zhu, S. Kaskel. *Microporous Mesoporous Mater* 2009, **118**, 176.

43. X. Wang, X. Li, A. Ito, Y. Sogo. *Acta Biomaterialia*. 2011, **7**, 3638.

44. J. Lacroix, J. Lao, E. Jallot. *J. Phys. Chem. C* 2013, **117**, 23066.

45. G.J.A.A. Soler-Illia, C. Sanchez, B. Lebeau, J. Patarin. J. *Chem. Rev.* 2002, **102**, 4093.

46. G.J.A.A. Soler-Illia, E.L. Crepaldi, D. Grosso, C. Sanchez. *Curr. Op. Coll. Inter. Sci.* 2003, **8**, 109.

47. H. Yamada, C. Urata, S. Higashitamori, Y. Aoyama, Y. Yamauchi, K. Kuroda. *ACS Appl. Mater. Interf.* 2014, **6**, 3491.

48. T. Suzuki, H. Miyata, M. Watanabe, K. Kuroda. *Chem. Mater*. 2006, **18**, 4888.

49. A. Shimojima, K. Kuroda. *J. Sol-Gel Sci Tech*. 2008, **46**, 307.

50. A. García, M. Cicuéndez, I. Izquierdo-Barba, D. Arcos, M. Vallet-Regí. *Chem. Mater.* 2009, **21**, 5474.

51. N. Letaïef, A. Lucas-Girot, H. Oudadesse, R. Dorbez-Sridi, P. Boullay. *Micropor Mesopor Mater* 2014, **195**, 102.

52. X. Yan, G. Wei, L. Zhao, J. Yi, H. Deng, L. Wang. *Micropor Mesopor Mater.* 2010, **132**, 282.

53. D. Arcos, D.C. Greenspan, M. Vallet-Regí. *J. Biomed. Mater. Res* 2003, **65A**, 344.

54. Y. Deng, X. Li, Q. Li. *Ind. Eng. Chem. Res*. 2009, **48**, 8829.
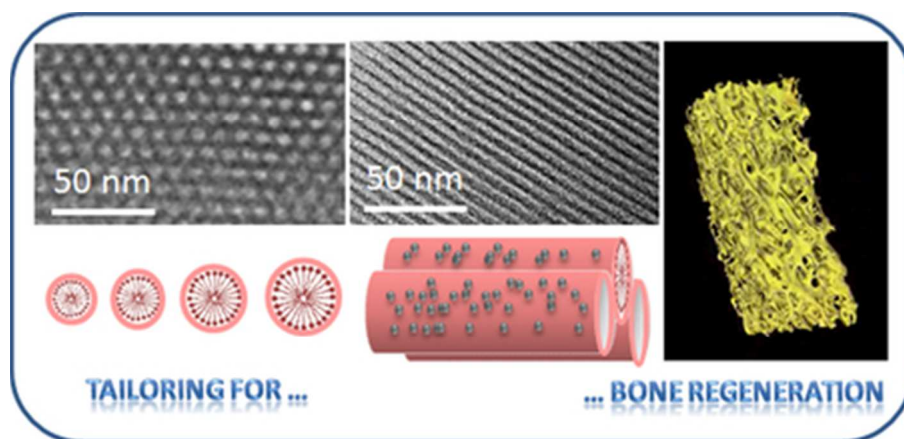
Mesoporous bioactive glasses can be tailored with structure directing agents to optimize their biological response
38x18mm (300 x 300 DPI)